



An efficient metal-free phosphorus and oxygen co-doped g-C₃N₄ photocatalyst with enhanced visible light photocatalytic activity for the degradation of fluoroquinolone antibiotics

Jiaxing Huang^a, Daguang Li^a, Ruobai Li^a, Qianxin Zhang^a, Tiansheng Chen^a, Haijin Liu^b, Yang Liu^c, Wenyang Lv^{a,*}, Guoguang Liu^{a,*}

^a School of Environmental Science and Engineering, Institute of Environmental Health and Pollution Control, Guangdong University of Technology, Guangzhou 510006, China

^b School of Environment, Henan Normal University, Key Laboratory for Yellow River and Huaihe River Water Environment and Pollution Control, Xinxiang 453007, China

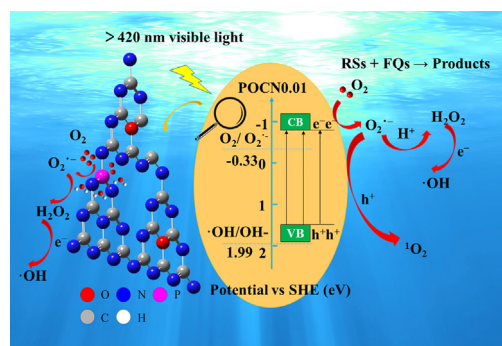
^c Faculty of Environmental & Biological Engineering, Guangdong University of Petrochemical Technology, Maoming 525000, China



HIGHLIGHTS

- A novel phosphorus and oxygen co-doped g-C₃N₄ (POCN) photocatalyst was prepared.
- The POCN showed excellent photocatalytic activity.
- The mechanism of the POCN photocatalyst was deduced.
- O₂^{•-} was the main reactive oxidative specie in the photocatalytic degradation.

GRAPHICAL ABSTRACT



ARTICLE INFO

Keywords:

Co-doped
g-C₃N₄
Fluoroquinolones
Mechanism
Pathway

ABSTRACT

Non-metal doping has been frequently used in g-C₃N₄ (CN) as a feasible and economical technique for maintaining its metal-free properties, while improving its photocatalytic performance. In this study, a novel phosphorus and oxygen co-doped graphitic carbon nitride (POCN) was successfully synthesized through a one-step thermal polymerization method and exhibited remarkable photocatalytic activity for the photocatalytic degradation of fluoroquinolones (FQs). The degradation rate of enrofloxacin (ENFX) was 6.2 times higher than that of CN. Based on the results of X-ray photoelectron spectroscopy (XPS) and nuclear magnetic resonance spectroscopy (NMR), P atoms replaced the corner and bay carbon sites, whereas O atoms replaced the nitrogen sites in the g-C₃N₄ framework. The improvement of the photocatalytic effect of POCN0.01 was attributed to its narrow bandgap, effective charge separation and enhanced specific surface area. This is the first report to describe the use of phosphorus doping to promote the generation of reactive oxygen species (ROS). ROS scavenging tests revealed that O₂^{•-} was the primary active species during the degradation of ENFX. Furthermore, pathways for the degradation of ENFX were proposed via the detection of intermediate products via HRAM LC-MS/MS and the prediction of active sites using the Fukui function.

* Corresponding authors.

E-mail addresses: lvwy612@163.com (W. Lv), liugg615@163.com (G. Liu).

<https://doi.org/10.1016/j.cej.2019.05.175>

Received 1 February 2019; Received in revised form 6 May 2019; Accepted 25 May 2019

Available online 27 May 2019

1385-8947/ © 2019 Elsevier B.V. All rights reserved.

1. Introduction

Fluoroquinolone antibiotics (FQs) are extensively employed for the treatment of bacterial infections in humans and animals on a global scale [1,2]. However, due to their stable chemical structures and recalcitrance to biological degradation, most of FQs cannot be effectively removed by conventional sewage treatment processes [3]. They have frequently been detected in wastewater and drinking water, which leads to the generation of drug-resistant bacteria and poses hazards to human health [4,5]. Conventional biotechnology and chemical oxidation strategies are time consuming, have low efficiency, and can easily produce secondary pollution. Therefore, effective strategies for the degradation of FQs have garnered strong interest.

In recent years, photocatalytic oxidation [6] has been regarded as an effective technique for the degradation of FQs. Many traditional photocatalysts (TiO_2) have shown excellent degradation capacities for the removal of FQs under UV light exposure [7]. However, TiO_2 absorbs UV light only, which limits its applications. As a non-metal polymeric photocatalyst, $g\text{-C}_3\text{N}_4$ (CN) has a narrow band gap of 2.7 eV [8,9]. Thus, it may serve as a visible light-driven photocatalyst for the degradation of environmental contaminants. Furthermore, the low toxicity, cost effectiveness and chemical stability of $g\text{-C}_3\text{N}_4$ makes it an interesting photocatalytic material [10]. However, the high recombination rate of photogenerated carriers, inefficient utilization of visible-light and small specific surface area of CN significantly limit its photocatalytic performance [8,11,12]. Therefore, many approaches have been explored to enhance the photocatalytic activity of CN, such as the design of unique morphologies [13,14], combination with other semiconductors (heterostructured photocatalysts) [15–17] and metal doping (Au [18], Fe [19], Ag [20], K [21]). Further, non-metal doping (B [22], F [23], C [24,25], P [26–28], S [29] and O [30,31]) is an economical and feasible method to maintain the metal-free properties of CN, while improving its photocatalytic performance. Due to the high ionization energies and high electronegativities of non-metals, they can form covalent bonds with electrons when they are used to dope CN. P-doped $g\text{-C}_3\text{N}_4$ (PCN) was successfully synthesized using a one-step thermal copolymerization method by Zhou et al. [32]. This research revealed that phosphorus atoms preferentially replaced the corner and bay carbon sites of CN, which caused a favorable electronic structure and suppressed the recombination rate of photogenerated electron-hole pairs. Although few insightful mechanisms were identified in the case of PCN. It was discovered that for other semiconductors modified with P, the promotion of O_2 adsorption occurred on TiO_2 , Fe_2O_3 , and BiOBr surfaces, and facilitated the formation of ROS. Li et al. initially synthesized O-doped CN using a facile H_2O_2 hydrothermal technique [33]. Up to now, many materials have been applied for the synthesis of O-doped CN (OCN) through thermal polycondensation, such as semicarbazide hydrochloride [13] and melamine with polyvinylpyrrolidone (PVP) [34]. These results revealed that oxygen atoms preferentially replaced the edge nitrogen atoms of CN. Further, OCN modulated the band structure, improved the specific surface area, visible light response and enhanced the separation efficiency of photogenerated electron-hole pairs.

However, co-doping enabled the combination of the merits of single doping agents. Recently, the co-doping of CN has garnered attention due to its positive structural and photometric influences. Hu et al. prepared phosphorus and sulfur co-doped $g\text{-C}_3\text{N}_4$ (PSCN) via in situ thermal condensation through the use of melamine, hexachlorotriphosphazene and sulfur. Phosphorus atoms were found to replace carbon atoms, whereas S atoms took the place of N atoms in the CN framework. The PSCN significantly enhanced the photocatalytic performance due to the N-S-N-C-N-P pathway, which accelerated charge transfer [35]. To the best of our knowledge, few studies have been conducted on the non-metal co-doped $g\text{-C}_3\text{N}_4$ polymeric materials for the degradation of FQs. Further, the degradation mechanism also lacks elucidation.

Herein, a visible light-driven photocatalyst (POCN) was synthesized via a one-step thermal condensation method, which demonstrated

excellent photocatalytic activity. Furthermore, the P and O occupied sites in the $g\text{-C}_3\text{N}_4$ were proposed. Enrofloxacin, ciprofloxacin, lomefloxacin and ofloxacin were tested to evaluate the photocatalytic performance of the photocatalysts. Additionally, enrofloxacin was selected to investigate the degradation kinetics involved. NMR, XPS and fourier transform infrared spectroscopy (FTIR) analyses were employed to study the POCN structure. The primary active species during the degradation of ENFX were presented based on the results of electron spin resonance (ESR) and reactive species trapping experiments. The degradation pathways of ENFX were deduced via the detection of intermediate products using HRAM LC-MS/MS and the prediction of reactive sites was proceeded using the Fukui function. Based on the above results, a mechanism to explain the excellent visible light-driven characteristics of the POCN was also proposed. This study served to demonstrate the enormous potential of non-metal co-doped $g\text{-C}_3\text{N}_4$ and promoted the further study of $g\text{-C}_3\text{N}_4$ -based photocatalysts.

2. Methods

2.1. Materials

Ciprofloxacin hydrochloride (CIP, 98%), lomefloxacin hydrochloride (NOR, 98%), enrofloxacin (ENFX, 98%), ofloxacin (OFL, 98%), guanidinium hydrochloride (GndCl, 98%), polyvinylpyrrolidone (PVP) and hexachlorotriphosphazene (HCCP, 98%) were purchased from Aladdin (America). HPLC-grade methanol was obtained from CNW Technologies GmbH (Germany).

2.2. Synthesis of photocatalysts

P-O co-doped $g\text{-C}_3\text{N}_4$ (POCN) was synthesized via a one-step thermal condensation technique, where 0.1 g PVP was dissolved in 100 mL water. Further, 5.0 g GndCl powder, 0.5 mL (0.01 wt%) PVP and 0.75 g HCCP were added to an alumina crucible, which contained 30 mL of deionized water. Subsequently, the mixture was evaporated at 75 °C under magnetic stirring to evaporate the deionized water and was dried in a convection oven at 75 °C for 12 h. Next, the dry powder was heated to 550 °C for 4 h at a ramp rate of 2 °C min^{-1} in a muffle furnace under ambient atmosphere. Once the photocatalysts were cooled to room temperature, they were ground into powder and then rinsed several times with distilled water for further use. The CN was synthesized with the addition of GndCl via the same method. The PCN and OCN were prepared by the identical method without the addition of HCCP and PVP, respectively. The photocatalysts and their raw materials are presented in Table S4 (Supporting information).

2.3. Characterization of photocatalysts

The structures of the samples were tested using X-ray diffraction (XRD, BRUKER D8 ADEVANCE), XPS (Thermo Fisher Scientific ESCALAB 250Xi), FTIR spectra (ThermoFisher Nicolet 6700 spectrophotometer) and NMR (600M, JNM-ECZ600R, Japan). UV-vis diffuse reflectance spectra were investigated using a UV-3600Plus UV-VIS-NIR spectrophotometer (Shimadzu). The morphologies of the products were investigated through scanning electron microscopy (SEM, SU8010), which was equipped with energy dispersive spectroscopy (EDS). The photoluminescence (PL) spectra and fluorescence lifetime were obtained via a transient steady-state fluorescence spectrometer, with an excitation of 350 nm (FS5, Edinburgh). The specific surface area and pore size distribution were quantified using a TriStar II 3flex (Micromeritics, USA). ESR spectroscopy of the solid samples were collected using a JES FA200 electron paramagnetic resonance spectrometer. The transient photocurrent responses and electrochemical impedance spectra (EIS) were measured using an electrochemical workstation (Multi Autolab/204, Metrohm) with a three-electrode quartz cell, in a 0.1 M Na_2SO_4 electrolyte solution (0.1 M).

2.4. Photocatalytic activity

Photocatalytic performance experiments for the CN, PCN, OCN and POCN were conducted through the degradation of ENFX under visible light. These tests were carried out in a rotary photochemical reactor (XPA-7, Nanjing Xujiang Machine-Electronic Plant). A 350 W xenon lamp with a 420 nm cut-off filter was employed as the visible light irradiation source. For each experiment, a 10 mg/L ENFX water solution (50 mL) containing 1.0 g/L catalysts was introduced into a 50 mL silica tube. Prior to light exposure, the reaction solution was magnetically stirred for 30 min to obtain the ENFX adsorption equilibrium. During the photocatalytic process, 1.0 mL samples were extracted every 20 min and filtered through 0.22 μm syringe filters to remove the photocatalyst. The filtrates were then examined via high performance liquid chromatography (HPLC, Waters, Alliance e2695-2998PDA). The degradation products of ENFX were detected by HRAM LC-MS/MS (Thermo Scientific™ Q Exactive™).

2.5. Determination of ROS during photocatalytic degradation

The primary ROS of the POCN detected during radical scavenging experiments were investigated through the addition of specific ROS scavengers prior to the photocatalytic process. The scavengers included 4-hydroxy-2,2,6,6-tetramethylpiperidinyloxy (TMPL) for the superoxide iron radical ($\text{O}_2^{\cdot-}$), isopropanol (IPA, 10 mM) for the hydroxyl radical ($\cdot\text{OH}$), sodium azide (NaN_3) for singlet oxygens, ($^1\text{O}_2$ and $\cdot\text{OH}$) and $\text{Na}_2\text{C}_2\text{O}_4$ for photogenerated holes (h^+), respectively. The ROS intensity was detected via ESR spectra (Bruker JES FA200).

2.6. Theoretical calculation

The structural geometries of ENFX were optimized by a M06-2X hybrid meta-GGA functional with a double split valence basis set 6-31 + G(d) through the Gaussian 09 program [36]. The solvent effects were considered by employing the integral equation formalism polarizable continuum model (IEFPCM). Fukui indices for nucleophilic or electrophilic attack were calculated based on Milliken and Hirshfeld algorithms, defined as the following formulas [37]:

$$f^+(r) = \rho_{N+1}(r) - \rho_N(r)$$

$$f^-(r) = \rho_N(r) - \rho_{N-1}(r)$$

$$f^0(r) = [\rho_{N+1}(r) - \rho_{N-1}(r)]/2$$

The corresponding (N - 1)-, N-, and (N + 1)-electron systems with the same molecular geometries were employed for independent calculations in the N electron system. Higher $f^+(r)$, $f^-(r)$, and $f^0(r)$ values translated to easier nucleophilic, electrophilic and radical attack in the functions, respectively.

3. Result and discussion

3.1. Characterization

The XRD patterns of the CN, PCN15, OCN0.01 and POCN0.01 are presented in Fig. 1a. The diffractograms revealed that all of the samples exhibited two typical diffraction peaks at 27.42° and 12.93°, which were attributed to the (0 0 2) and (1 0 0) crystal planes of CN [38]. The (0 0 2) crystal face was associated with the interlayer distance and the (1 0 0) crystal face was associated with an in-plane structural motif of the $\text{g-C}_3\text{N}_4$ [39]. For the PCN samples, the 002 of the PCN was barely changes with doping, indicating that the interplanar distance was not affected by the presence of P. However, the shift of the (0 0 2) peak was found for the OCN samples (27.42°–27.77°), which indicated structural compression following O doping. This implied that the interactions between the graphitic carbon nitride sheets were enhanced due to the O

atoms possessing stronger electronegativity than N atoms [34]. The (1 0 0) did not reveal any peak shifting, which meant that the PCN, OCN, and POCN retained their tri-s-triazine units.

FTIR spectra was used to detect the bonding characteristics of CN, PCN15, OCN0.01 and POCN0.01 (Fig. 1b) [40]. The peak at 810 cm^{-1} was attributed to the breathing mode of a heptazine unit, whereas 1200–1700 cm^{-1} corresponded to the C–N heterocycle system [41]. The peaks at 1240, 1318 and 1573 cm^{-1} represented the C–NH–C, C–N and C=N bonding in melam, respectively [42]. The peaks in the range of from 3000 to 3500 cm^{-1} corresponded to C–OH and N–H (adsorbed H_2O molecules and uncondensed amine groups) [43]. These results indicated that the synthesized CN, PCN15, OCN0.01 and POCN0.01 samples were comprised of a 3-s-triazine ring structure, which was the same as the XRD results. However, no other peaks were detected following P and O doping due to the low doping content.

Furthermore, the chemical binding and oxidation states of the POCN0.01, PCN15, OCN0.01 and CN samples were examined by XPS. Fig. S1a shows the survey spectra of C 1s, N 1s, P 2p and O 1s of the CN, PCN15, OCN0.01 and POCN0.01 samples. High-resolution C 1s, O 1s, N 1s and P 2p spectra are shown in Fig. 2a–d. Three peaks at 284.4, 287.5 and 285.6 eV were observed in all of the samples (C 1s), which could be assigned to C=C, C–N=C [44] and C–O [45], respectively (Fig. 2b). The N 1s XPS spectra of CN, located at 397.7, 399.0 and 400.4 eV were attributable to C–N=C, N–(C)₃ and N–H, respectively [46] (Fig. 2c). These C 1s and N 1s XPS spectra results further confirmed the triazine heterocyclic ring structure of the CN, PCN15, OCN0.01 and POCN0.01. The peak at 134.10 eV was found in the XPS spectra of P 2p, which was attributed to the P–N (Fig. 2a) [47,48]. Phosphorus atoms substituted carbon atoms to form covalent bonds with adjacent nitrogen atoms in the heptazine units of PCN15. The O 1s XPS spectra of the CN exhibited two peak at 531.9 and 533.2 eV, which could be attributed to O–H (molecular water) and C=O [49,50]. However, a new peak at 532.8 eV was observed in the OCN and POCN materials, which was assigned to the C–O–C species [51,52] (Fig. 2d). It was suggested that oxygen atoms replaced nitrogen atoms and bonded with adjacent nitrogen atoms in the OCN0.01 and POCN0.01. The binding energy in the C1s, N1s, O1s and P 2p region shifted in PCN15, OCN0.01 and POCN0.01, which indicated that P and O doping altered the chemical environment of the C, N, O and P atoms. As shown in Fig. S1d, the O 1s XPS spectra of the PCN15 exhibited a strong peak at 531.5 eV, which was ascribed to molecular water.

Solid-state ^{13}C and ^{31}P magic angle spinning (MAS) NMR were tested to verify the internal $\text{g-C}_3\text{N}_4$ structures. As can be seen in Fig. 3b, the ^{31}P NMR analysis of the PCN15 sample revealed three well-resolved peaks between +10 ppm and –20 ppm (asterisks in figure). The peaks at –9.1 and –11.0 ppm were assigned to the corner and bay phosphorus sites in the heptazine units of $\text{g-C}_3\text{N}_4$ [4]. Further, the peak at +1.5 ppm was attributed to the formation of P=O at the edge of $\text{g-C}_3\text{N}_4$ [32]. Similar peaks were also found in the POCN0.01, where the weak signal and peak shifts were influenced by O doping. As seen in Fig. 3a, the ^{13}C NMR spectra of the CN, PCN15 and POCN0.01 exhibited two similar signals (157.3 (1) ppm and 165.3 (2) ppm), which were assigned to the CN_3 (1) and CN_2NH_2 (2) groups [53–55], respectively. The additional signals at ~156.1 (5) ppm appeared in the CN sample, which were attributed to the formation of C=O at the terminal edge locations. Compared with CN, a small split was found in the signals for 158.0 (3) and 165.7 (4) ppm of the OCN0.01 and POCN0.01, due to the formation of C–O–C at this position [13]. Based on the above results, P atoms replaced the corner and bay carbon sites, whereas O atoms replaced the nitrogen sites in the $\text{g-C}_3\text{N}_4$ framework.

SEM mages (Fig. 4a–d) of the CN, PCN15, OCN0.01 and POCN0.01 samples, respectively, elucidated their surface morphologies and microstructures. As can be seen in the SEM images, the CN sample exhibited a typical blocky stacked structure (Fig. 4a). Moreover, with P and O doping, the PCN, OCN and POCN materials became fragmented and rough due to the increase in gas produced during the reaction of

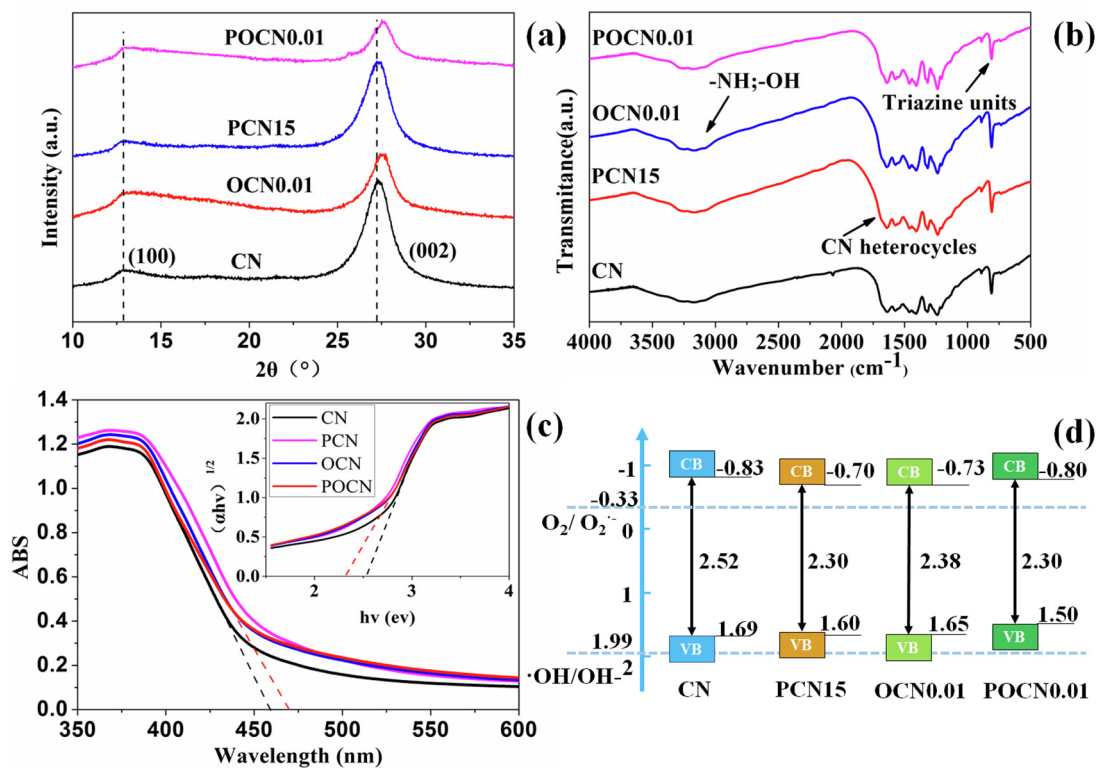


Fig. 1. (a) XRD patterns, (b) FTIR spectra, (c) The UV-vis diffuse reflectance absorbance spectra and (d) band gap of CN, PCN15, OCN0.01 and POCN0.01.

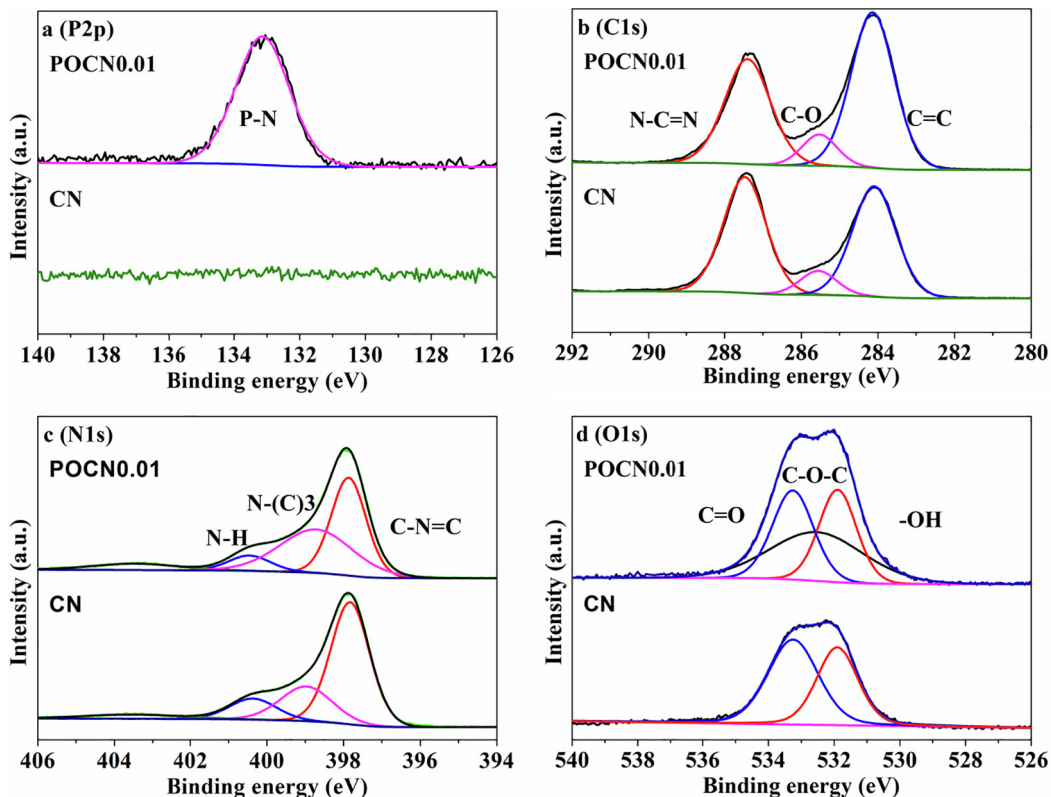


Fig. 2. XPS analysis of CN and POCN0.01: (a) P 2p spectra, (b) C 1s spectra, (c) N 1s spectra, (d) O 1s spectra.

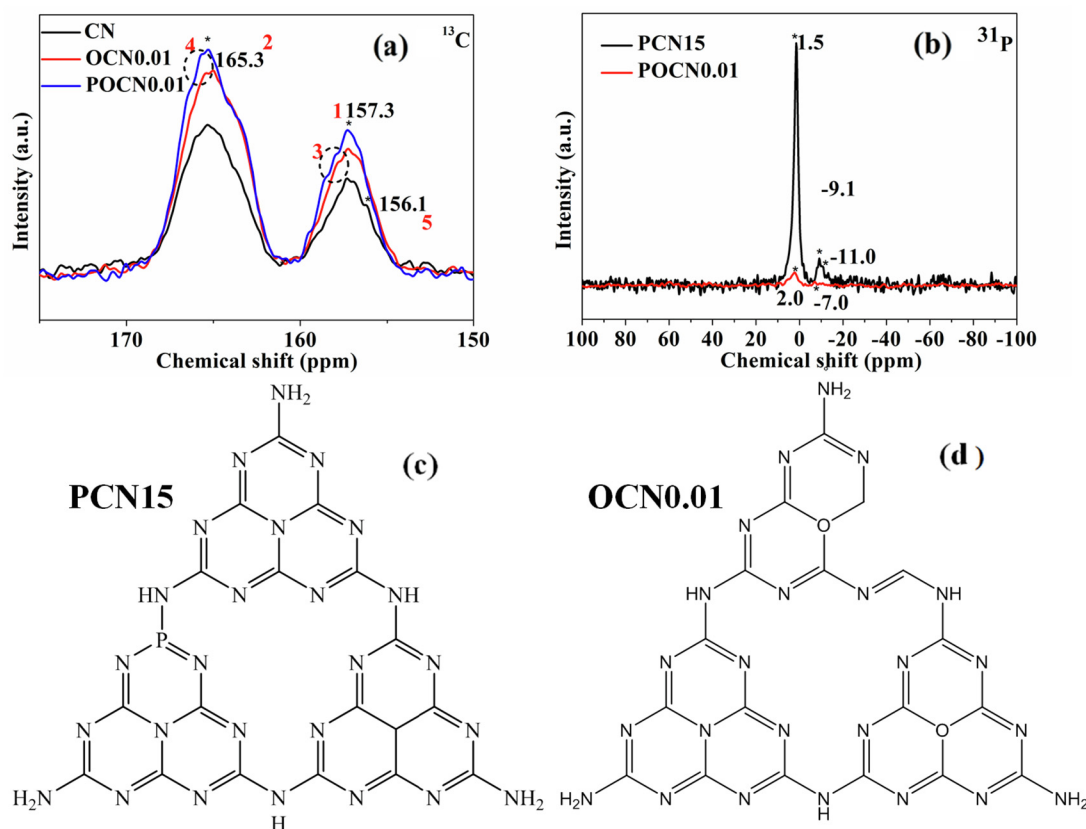


Fig. 3. (a) ^{13}C MAS NMR spectra of CN, OCN0.01 and POCN0.01, (b) ^{31}P solid-state MAS NMR spectra of PCN15 and POCN0.01, (c) and (d) structures of PCN15 and OCN0.01.

guanidinium hydrochloride with PVP and by-products during the reaction of GndCl and HCCP (Fig. 4b–d). The N_2 adsorption-desorption isotherms for the CN and POCN0.01 samples were shown in Fig. S6. It presented a type II isotherm with narrow hysteresis loops, which is the character in mesoporous materials [56]. The BET specific surface area of POCN0.01 was $50.71 \text{ m}^2/\text{g}$, which was ~ 1.4 times higher than the CN. The increased specific surface area of POCN sample was due to the gas produced during the reaction of guanidinium hydrochloride with PVP, which promoted the formation of the porous structure. Furthermore, the average pore size of the POCN0.01 was 22.70 nm , which was smaller than the CN ($\sim 27.20 \text{ nm}$). In addition, the pore volume of the POCN0.01 attained $0.253 \text{ cm}^3/\text{g}$ and the CN sample was $0.215 \text{ cm}^3/\text{g}$. All findings indicated that the POCN0.01 had a larger specific surface area, which was beneficial for mass transfer, photocatalytic adsorption and ROS attack. To determine the chemical composition of the POCN0.01 sample, elemental analyses were tested by EDS which was a component of the SEM. It was obvious that both P and O were evenly dispersed on the POCN0.01 nanoparticles. The results of elemental analysis (EA) revealed the C/N ratios for CN, PCN15, OCN0.01 and POCN0.01, which are displayed in Table 1. The CN, PCN15, OCN0.01 and POCN0.01 had C/N ratios of 0.663, 0.669, 0.666 and 0.677, respectively. These results deviated from the ideal 0.75 (C_3N_4) due to the amino groups originated from the incomplete condensation, which was in agreement with the FTIR and XPS results [57,58]. However, the PCN15 sample exhibited increased C/N ratios following P doping, which suggested that P doping could inhibit the formation of the amino groups. Further, the C/N ratios were increased following O doping, which implied that O replaced N in $\text{g-C}_3\text{N}_4$ [34]. Furthermore, the C/N ratios of POCN increased subsequent to P-O doping, which further confirmed the above inference, in contrast to PCN15 and OCN0.01.

The light absorption capacity and band gap energy of the CN, PCN15, OCN0.01 and POCN 0.01 were observed using UV–vis diffuse

reflectance spectra. As shown in Fig. 1c, the CN sample exhibited an absorption edge at $\sim 460 \text{ nm}$. In addition, an absorption edge extending to 470 nm was detected in the POCN0.01 sample. The optical band gaps of CN, PCN15, OCN0.01 and POCN0.01 were calculated according to Eq. (1):

$$\alpha h\nu = A(h\nu - E_g)^{n/2} \quad (1)$$

where α , h , ν , A and E_g corresponded to the absorption coefficient, Planck's constant, light frequency, a constant and band gap energy [59,60], respectively. The indirect gap energies of the CN, PCN15, OCN0.01 and POCN0.01 samples are revealed in the illustration of Fig. 1c. The indirect band gap energies of CN, PCN15, OCN0.01 and POCN0.01 were estimated to be 2.52, 2.30, 2.35 and 2.30 eV, respectively. As anticipated, the band gap energies were observed to decrease subsequent to P and O doping. The bandgap narrowing of the PCN and POCN samples were due to the valence electrons at the P 2p level. Moreover, P doping in the electronic band created several occupied impurity bands in the $\text{g-C}_3\text{N}_4$ [35]. Furthermore, the narrowing band gap of OCN0.01 could be ascribed the positive-shift of the conduction band following O doping. The valence band (VB) of CN, PCN15, OCN and POCN were determined using valence band X-ray photoelectron spectroscopy (VB-XPS). As shown in Fig. S2, the valence band (VB) position of CN, PCN15, OCN0.01 and POCN0.01 were estimated to be 1.69, 1.60, 1.65 and 1.50 eV via the VB-XPS spectrum. Moreover, the CB positions of the CN, PCN, OCN and POCN samples were determined to be -0.83 , -0.70 , -0.73 and -0.80 eV according to the empirical formula: $E_{\text{VB}} = E_{\text{CB}} + E_g$. The energy band structures of these materials are shown in Fig. 1d. The VB of POCN0.01 was negative-shifted following to P and O co-doping.

Steady-state photoluminescence (PL) spectra were employed to uncover the recombination rate of photogenerated electron-hole pairs [61]. As can be seen in Fig. 5c, the emission intensity of PCN15,

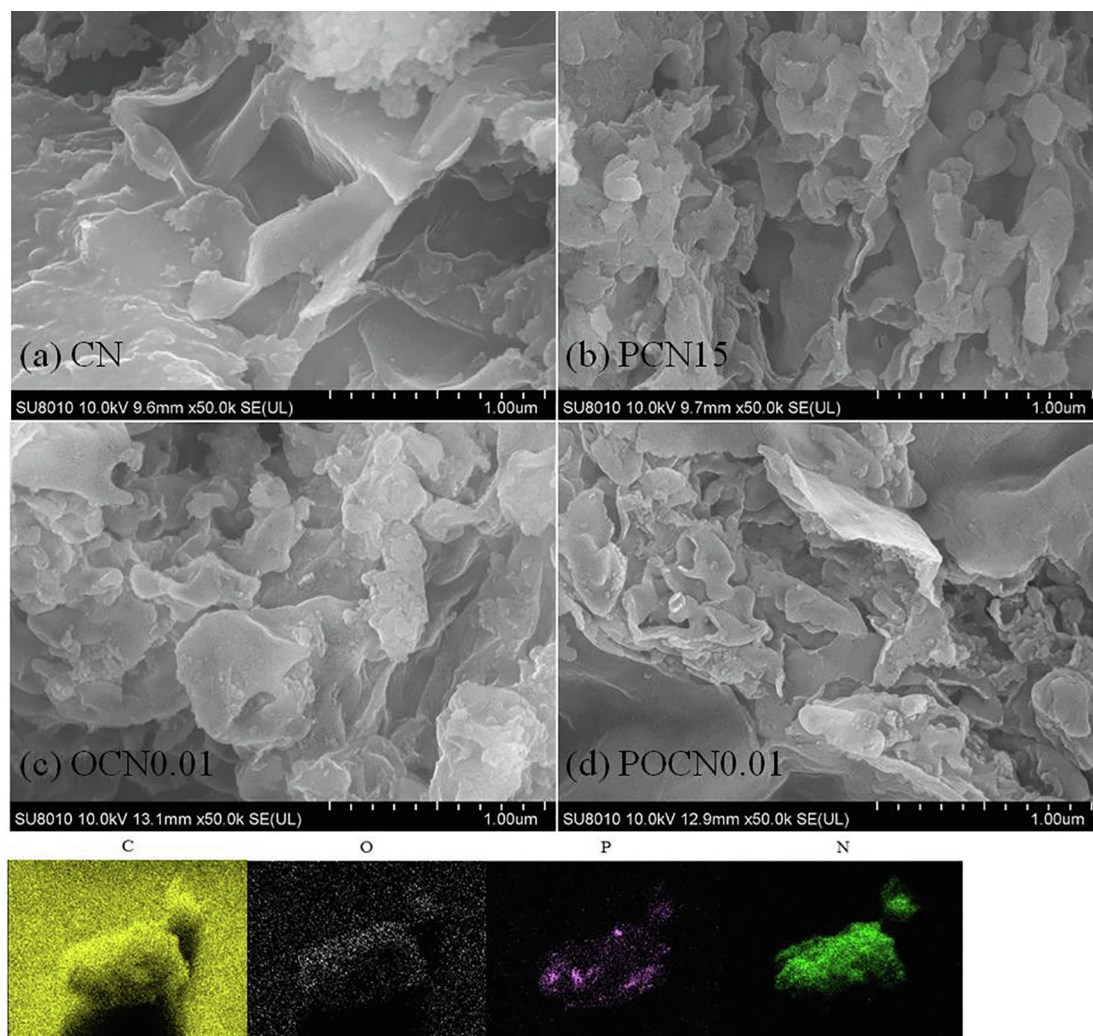


Fig. 4. SEM images of CN (a), PCN15 (b), OCN0.01 (c) and POCN0.01 (d); EDS mapping images of POCN0.01.

Table 1

The results of EA.

Samples	N (wt%)	C (wt%)	H (wt%)	C/N
CN	53.083	30.159	1.680	0.662839
PCN15	58.418	33.472	1.866	0.66847
OCN0.01	59.928	34.197	1.850	0.665741
POCN0.01	59.449	34.480	1.933	0.676658

OCN0.01 and POCN0.01 exhibited an obvious decrease in contrast to CN. To quantify the lifetimes of the charge carriers, time-resolved PL tests were conducted. The emission peaks were at 445 nm (CN), 473 nm (PCN15), 465 nm (OCN0.01) and 466 nm (POCN0.01), respectively. The average lifetimes of CN, PCN15, OCN0.01 and POCN0.01 samples were 4.950, 4.588, 4.511 and 4.429 ns as shown in Fig. 5d and Table S2, respectively. The decreased average lifetime indicated that once oxygen atoms replaced nitrogen atoms (phosphorus replaced the carbon atoms), the recombination of electron-hole pairs were effectively suppressed in the PCN15, OCN0.01 and POCN0.01 [16,34]. When the P atoms replaced C atoms, the lone electron pairs from the P atoms delocalized to the P doped triazine ring. The intrinsic P–N bond polarization and lone electron delocalization resulted in the generation of P + center (Lewis acid sites), which promoted the separation of photo-generated electron-hole pairs [43,62]. When O atoms replaced N atoms, the lone electron pairs of O atoms were delocalized to the oxygen-doped aromatic system, which increased the charge density and

mobility [63]. Besides, the lattice strain from changes in the C–N bond lengths and electronic polarization effects facilitated the formation of an internal electric field, which favored electron-hole separation [30].

Furthermore, a doubling of the photocurrent was recorded by transient photocurrent responses and the low electrochemical impedance of POCN0.01 confirmed that the charge transport was improved following co-doping. These two properties were also enhanced in the PCN15 and OCN0.01 (Fig. 5a and b).

3.2. Photocatalytic performance

The photocatalytic activities of the designed photocatalyst were tested via the degradation of FQs under simulated visible light irradiation, enrofloxacin (ENFX), ciprofloxacin, lomefloxacin and ofloxacin. As presented in Fig. 6a, the ENFX solution containing the photocatalysts was magnetically stirred in the dark for 30 min until the adsorption equilibrium was attained. As can be seen in Fig. 6a, an excess of P and O in the composites would inhibit the photocatalytic properties. The photocatalytic performance of the material to achieve the best when the addition amount of the phosphorus source and a source of oxygen 15% and 0.01%. As shown in Fig. 6b, the degradation rate constants of CN reached 0.0038 min^{-1} . Moreover, once the CN sample was doped with P or O, the degradation rates of the PCN15 and OCN0.01 were 0.0042 and 0.076 min^{-1} , which was appreciably enhanced in contrast to CN. Moreover, the POCN0.01 demonstrated the best degradation effect, and the photocatalytic activity of the POCN0.01

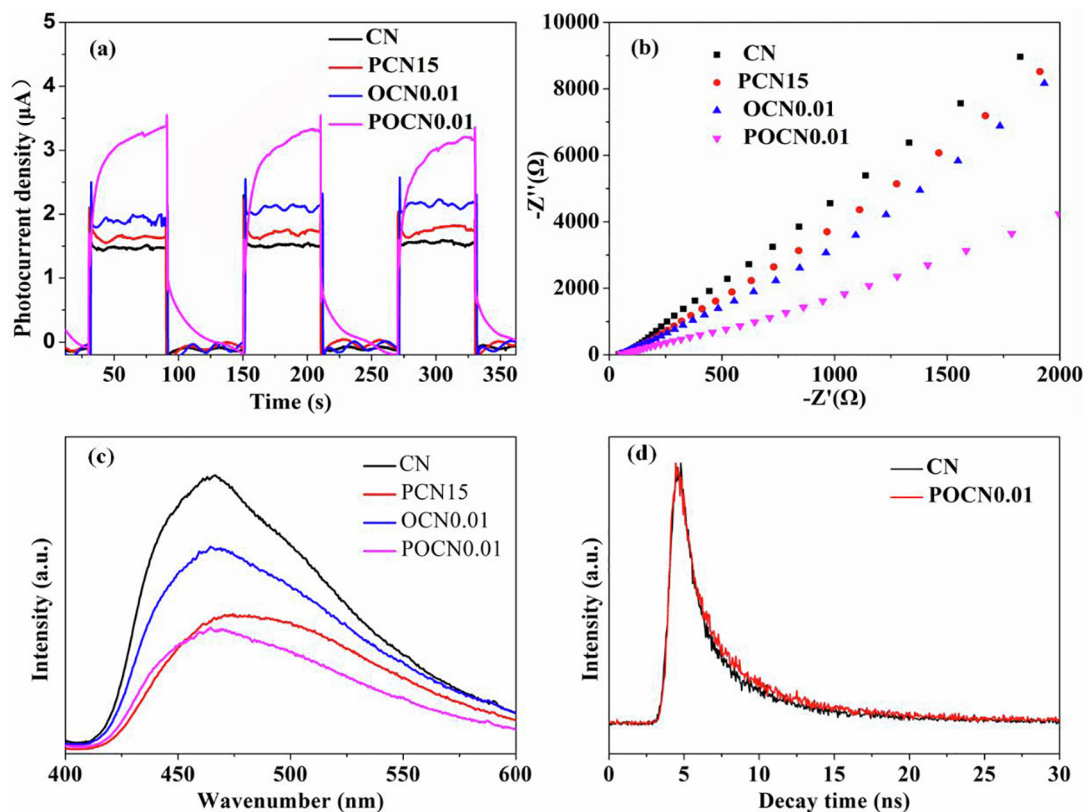


Fig. 5. (a) Photocurrent responses, (b) electrochemical impedance spectra, (c) Photoluminescence spectra of CN, PCN15, OCN0.01 and POCN0.01, (d) fluorescence decay of CN and POCN0.01.

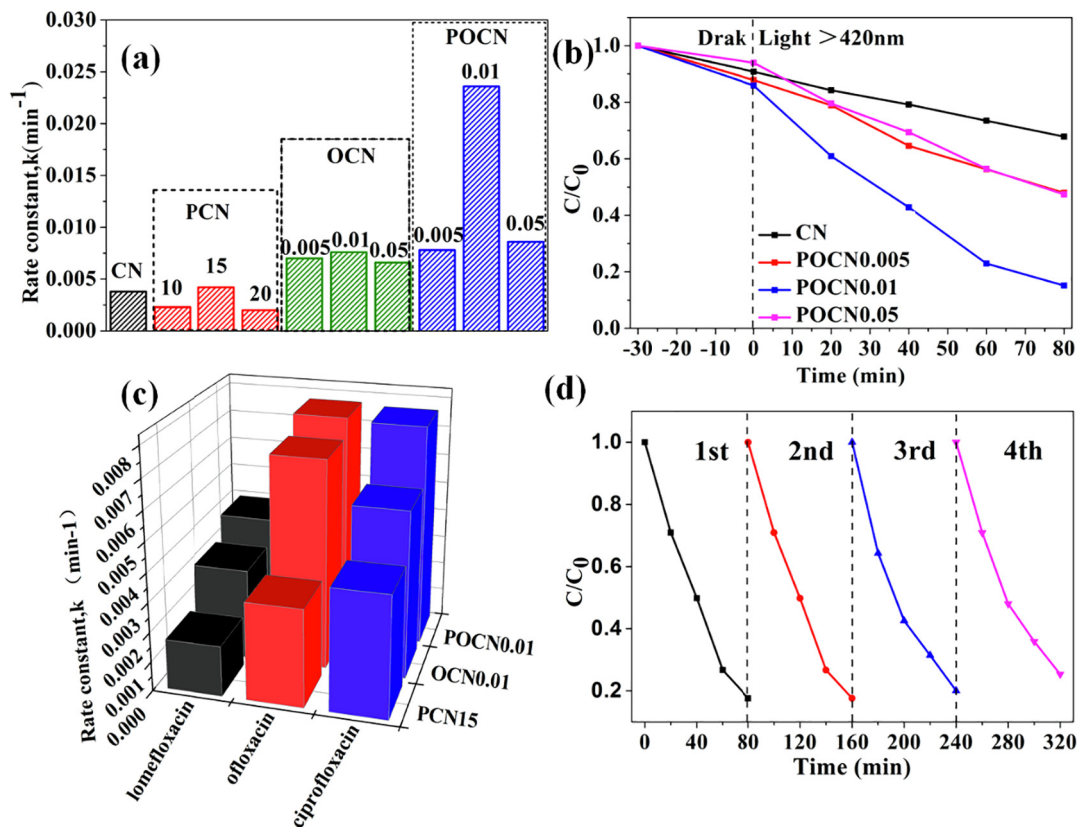


Fig. 6. (a) Photocatalytic degradation of ENFX with different photocatalysts under visible light irradiation; (b) Kinetic rate constant of ENFX degradation over different photocatalysts; (c) Photocatalytic degradation of FQs under visible light irradiation. (d) Photocatalytic degradation activity after three cycles of POCN0.01 photocatalyst under visible light irradiation.

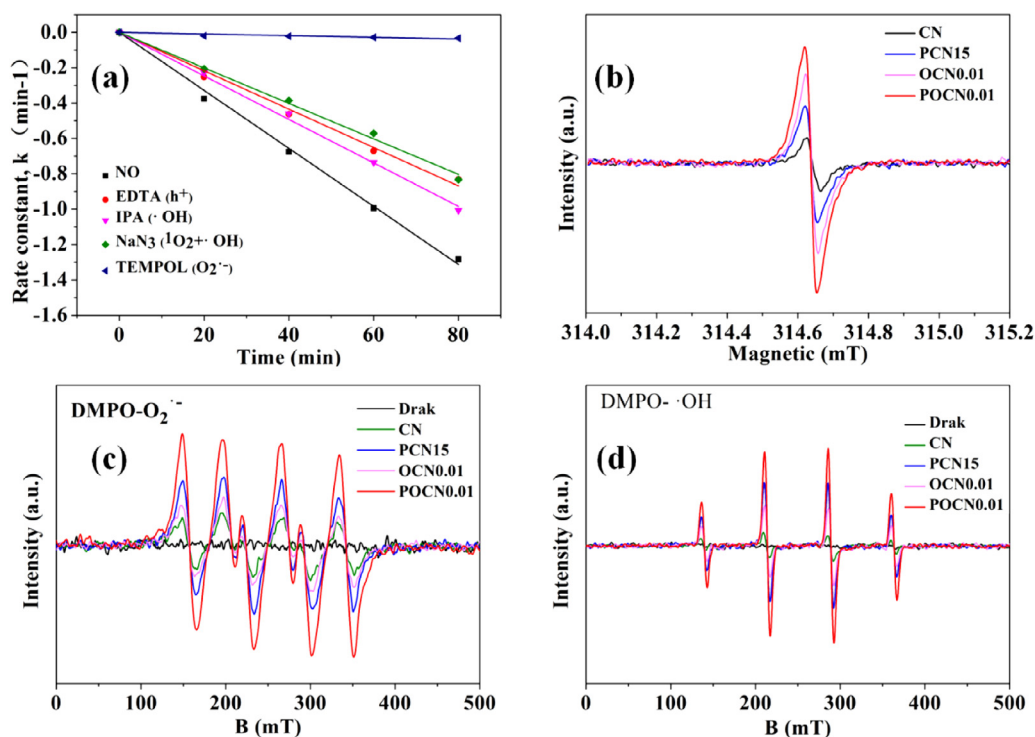


Fig. 7. (a) Photocatalytic degradation of ENFX under visible light irradiation with addition of different scavengers using POCN0.01 photocatalyst. (b) Room-temperature ESR spectra of CN, PCN15, OCN0.01, and POCN0.01 under visible light irradiation. The ESR spectrum of DMPO/·OH and O₂^{·-} in the presence of CN, PCN15, OCN0.01, and POCN0.01.

(0.0236 min⁻¹) was 6.2 times higher than that of CN. The same phenomenon is depicted in Fig. 6c, where the degradation rates of ciprofloxacin, lomefloxacin and ofloxacin with these photocatalysts were in the order of POCN0.01 > OCN0.01 > PCN15 > CN. This confirmed that P and O co-doping is a viable method for enhancing the photocatalytic degradation of FQs.

3.3. Photocatalytic mechanism

To identify the primary reactive species involved in the photocatalytic degradation of ENFX, scavenger tests were conducted by introducing different scavenger species into the photocatalytic reactions. Holes (h⁺), hydroxyl radicals (·OH) and superoxide radicals (O₂^{·-}) were quenched by ethylenediaminetetraacetate (EDTA-2Na), isopropanol (IPA) and 4-hydroxy-2, 2, 6, 6-tetramethylpiperidinyloxy (TEMPOL), respectively. In particular, sodium azide (NaN₃) served as a hydroxyl radical (·OH) and singlet oxygen (¹O₂) scavenger. As seen in Fig. 7a, the reaction rate constant of ENFX were decreased following the addition of TEMPOL, IPA, EDTA-2Na and NaN₃. The inhibition rates of O₂^{·-}, ·OH and h⁺ were calculated to be 96.9%, 22.6% and 34.6%, respectively. As was expected, O₂^{·-} played a decisive role in the photocatalytic degradation of ENFX under visible light irradiation.

Room-temperature ESR was tested to obtain further evidence relative to the structural alternation due to P and O doping. In Fig. 7, the single Lorentzian lines are shown in the CN, PCN15, OCN0.01 and POCN0.01, which ranged from 314.5 to 314.8 mT. The value of g (1.999) was attributed to the uncoupled electrons in the π -bonded aromatic rings of g -C₃N₄ [61,64]. As anticipated, the ESR intensity of PCN15, OCN0.01 and POCN0.01 were greatly enhanced. Compared with N atoms, O atoms possessed extra electrons, which were transported to adjacent C atoms and delocalized among the large π bonds of the g -C₃N₄, when O atoms replaced N atoms during the calcination process [16]. Further, the substituting C atom in the heptazine unit with a P atom also facilitated the increase of unpaired electrons in the g -C₃N₄. Therefore, the unpaired electrons in the POCN0.01 polymer were notably increased following to P and O doping.

Moreover, the ESR spectra was used with the trapping agents to determine the quantity of ROS that were present during the

photocatalytic degradation. As shown in Fig. 7c and d, no O₂^{·-} or ·OH radical signals of CN, PCN, OCN and POCN were detected under dark conditions. However, it was obvious that the apparent signals of DMPO-O₂^{·-} and DMPO·OH were detected in CN, PCN15, OCN0.01 and POCN0.01 under the visible-light irradiation. The signal intensity of DMPO-O₂^{·-} with POCN, OCN, PCN and CN catalysts were in the order of POCN0.01 > PCN15 > OCN0.01 > CN. It was intriguing to discover the same phenomenon in the DMPO·OH signal. It indicated that P and O doping benefited the yield of O₂^{·-} and ·OH radicals in the POCN photocatalytic system [65]. However, the photocatalytic activity of the ENFX degradation by OCN was improved over PCN. This was likely due to the improved ENFX adsorption performance of the OCN0.01. Compared with the results of ESR (unpaired electrons), an interesting phenomenon was found. Although the PCN15 possessed fewer unpaired electrons than the OCN0.01, it generated additional ·OH and O₂^{·-}. This meant that O₂ reacted with unpaired electrons and generated ROS more easily at the surface of the PCN15. The same phenomenon was also found in phosphate-modified BiOBr nanoplates. This photocatalytic material enhanced the adsorption of O₂ so as to promote captured electrons toward the generation of ROS [66].

As is well known, the VB of POCN0.01 (+1.50 eV) was more negative than the potential of ·OH/OH⁻ (+1.99 eV vs. NHE) and ·OH/H₂O (+2.27 eV vs. NHE) [67], which indicated that the photo-holes could not directly oxidize OH⁻/H₂O to the active ·OH species [68]. Hence, based on the above results and previous research, the probable photocatalytic mechanisms of the photodegradation of ENFX were proposed and are shown in Eqs (2)–(7) [13].

The photogenerated electrons on the CB of POCN0.01 reacted with oxygen to generate O₂^{·-}, as the CB potential of POCN0.01 was more negative than the E₀ (O₂/O₂^{·-}, -0.33 eV) [7]. Subsequently, the O₂^{·-} reacted with water to form H₂O₂, and ·OH could be generated through the reaction of photogenerated electrons with H₂O₂ [14]. Further, ¹O₂^{·-} could react with h⁺ to generate ¹O₂ [10]. The h⁺ could easily attack ENFX molecules and O₂^{·-}, ·OH and ¹O₂ radicals degraded intermediate products into CO₂ and H₂O [65].



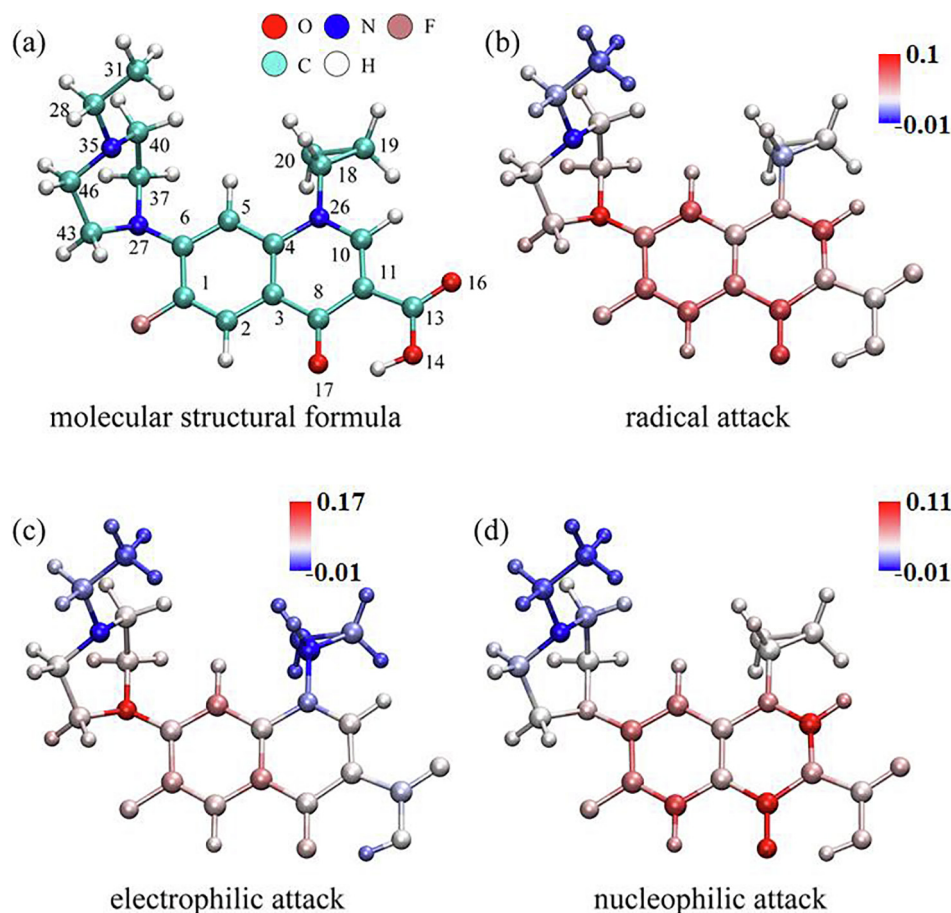
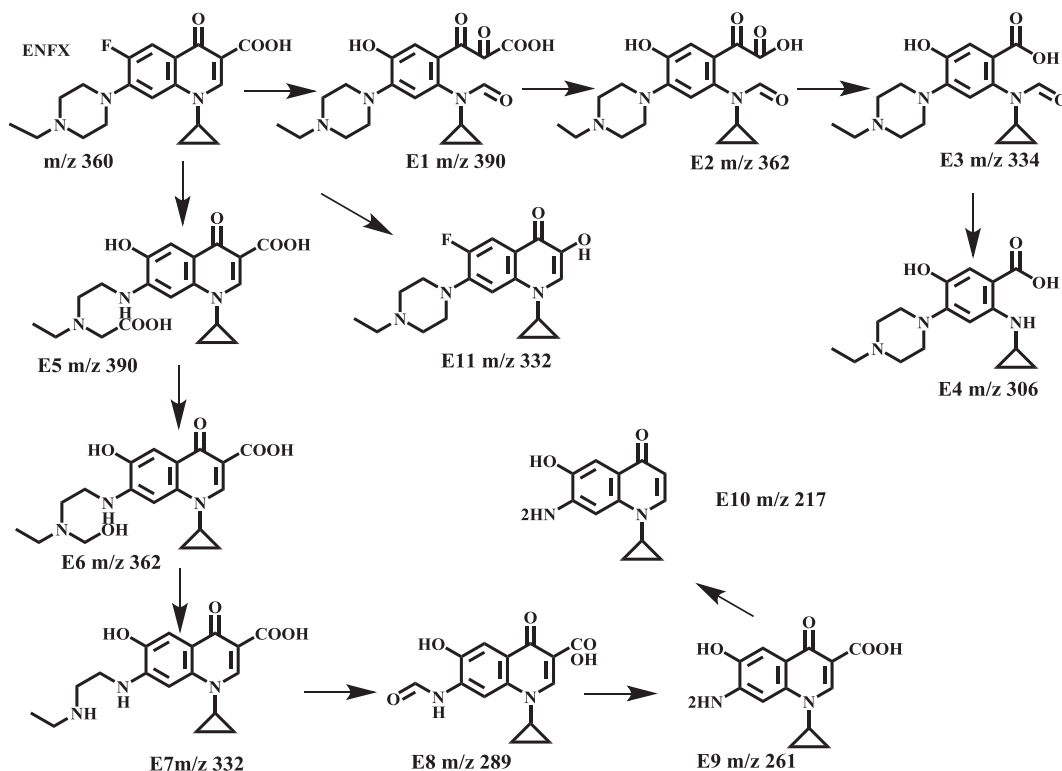
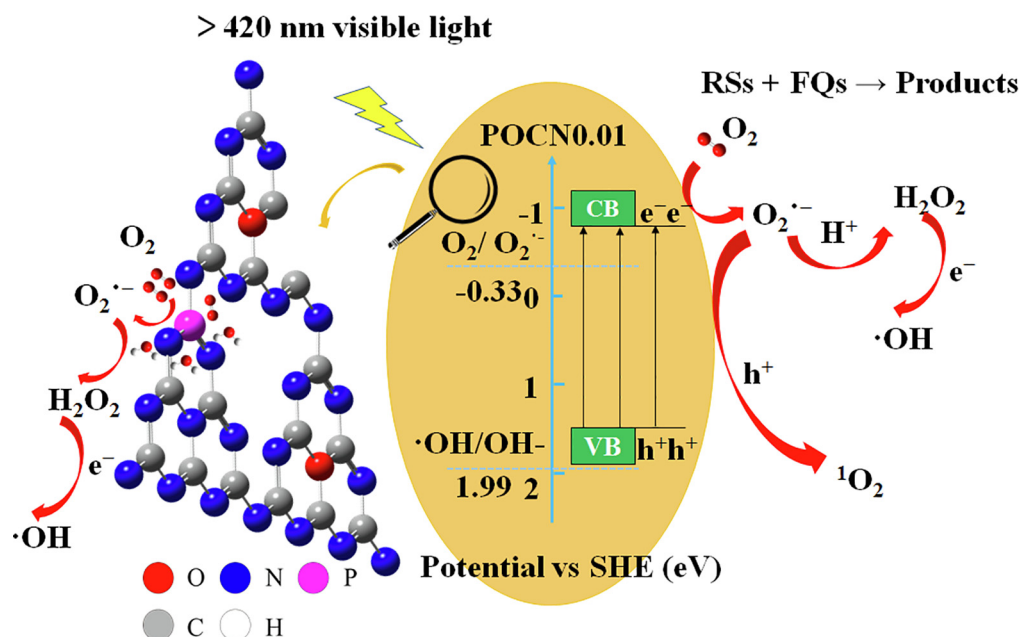


Fig. 8. Structural formula of ENFX: (a) optimized structure and atom number, (b)–(d) the atomic coloring schemes of ENFX with different values of $f^0(r)$, $f^-(r)$ and $f^+(r)$. (For interpretation of the references to colour in this figure legend, the reader is referred to the web version of this article.)



Scheme 1. Potential photocatalytic degradation pathways of ENFX in POCN0.01 aqueous solution under visible light irradiation.



3.4. Degradation pathway

The intermediate products determined by HRAM LC-MS/MS were utilized during the photocatalytic degradation of ENFX. Fig. S3 shows the secondary mass spectrometry of the twelve by-products that were identified by HRAM LC-MS/MS. Furthermore, Fukui functions were utilized to predict the active sites for ROS attack [69,70]. The optimized structure and atomic numbering of enrofloxacin are shown in Fig. 8a. According to the atomic coloring schemes with different values of $f^+(r)$, $f^-(r)$ and $f^0(r)$ (Fig. 8b-d), N27 was a suitable site for electrophilic attack. The C8, C10 and O17 atoms of ENFX exhibited higher $f^+(r)$ values (Fig. 8d), which indicated that these sites were more easily to the nucleophilic addition reactions [65]. In addition, C1, C2, C3, C5, C8, C10, O17 and N27 were easily attacked by radicals due to their higher $f^0(r)$ values [71,72]. A typical ion spectrum of ENFX ($m/z = 360.2$) was detected at $RT = 8.17$ min. The ion spectra of intermediate products were detected in a positive ion model. Further, the proposed photocatalytic degradation pathways of ENFX were predicted in Scheme 1. Three potential primary degradation pathways are shown as follows: The substitution of a fluorine atom by a hydroxyl group and the opening of quinolone moieties occurred in Pathway I. Firstly, a hydroxyl group replaced the fluorine atom in ENFX and formed the product E1 under the attack of $\cdot OH$ radicals. Subsequently, the quinolone moieties were destroyed by the $O_2^{\cdot-}$, h^+ and $t \cdot OH$ radicals, which in turn generated the compound E2-E4. A similar pathway was reported in previous studies [73]. Pathway II included the substitution of a fluorine atom by a hydroxyl group and the loss of a piperazinyl group. The fluorine atom was displaced by a hydroxyl group, after which the piperazine ring was attacked and oxidized to generate the product E5. Subsequently, the E5 lost the carbonyl group to form E6, which was further transformed to E7 by losing the $-OH$ and $-CH_2$

group. E7 was further oxidized to generate E8, which lost the carbonyl group again and changed to E9. Similarly, the decarboxylation process was also presented in previous reports [74]. E9 was further transformed EFA 10 through decarboxylation. This pathway was similar to the degradation of ciprofloxacin as described by Jiang et al. [75]. Pathway III primarily involved decarboxylation and the opening of quinolone moieties. C13 was attacked by $O_2^{\cdot-}$, and the decarboxylation occurred at the quinolone groups of ENFX, as it possessed a partial positive charge. The product E11 was formed through this pathway (Scheme 2).

4. Conclusion

A non-metal POCN was synthesized through the combination of hexachlorocyclotriphosphazene (HCCP) and polyvinylpyrrolidone (PVP) via a one-step thermal polymerization process. Compared to CN, this photocatalyst exhibited remarkable performance toward the degradation of fluoroquinolone (FQ) due to a wider light absorption range, quenched photocarrier recombination and lower electronic resistance. It was observed that $O_2^{\cdot-}$ radicals played significant roles in the photocatalytic degradation of ENFX under the visible light. Moreover, phosphorus doping promoted the generation of reactive oxygen species (ROS) due to its excellent oxygen absorbency. The degradation pathways of ENFX were predicted via the identification of intermediates using HRAM LC-MS/MS and the prediction of active sites by the Fukui function. Moreover, this research might expand the applications of efficacious photocatalysts for sewage treatment and water purification, while providing a new strategy for the facile and convenient synthesis of advanced photocatalysts.

Acknowledgments

This work was supported by National Natural Science Foundation of China (No. 21677040 and 21377031) and the Science and Technology Planning Project of Guangdong Province (No. 2017A050506052).

Appendix A. Supplementary data

Supplementary data to this article can be found online at <https://doi.org/10.1016/j.cej.2019.05.175>.

References

- [1] T. Paul, M.C. Dodd, T.J. Strathmann, Photolytic and photocatalytic decomposition of aqueous ciprofloxacin: Transformation products and residual antibacterial activity, *Water Res.* 44 (2010) 3121–3132.
- [2] D.C. Hooper, J.S. Wolfson, Fluoroquinolone antimicrobial agents, *N. Engl. J. Med.* 324 (1991) 384–394.
- [3] T. Paul, P.L. Miller, T.J. Strathmann, Visible-light-mediated TiO₂ photocatalysis of fluoroquinolone antibacterial agents, *Environ. Sci. Technol.* 41 (2007) 4720–4727.
- [4] Y. Zhang, T. Mori, J. Ye, M. Antonietti, Phosphorus-doped carbon nitride solid: enhanced electrical conductivity and photocurrent generation, *J. Am. Chem. Soc.* 132 (2010) 6294–+.
- [5] C. Liu, V. Nanaboina, G.V. Korshin, W. Jiang, Spectroscopic study of degradation products of ciprofloxacin, norfloxacin and lomefloxacin formed in ozonated wastewater, *Water Res.* 46 (2012) 5235–5246.
- [6] Y. Ye, Z. Zang, T. Zhou, F. Dong, S. Lu, X. Tang, W. Wei, Y. Zhang, Theoretical and experimental investigation of highly photocatalytic performance of CuInZnS nanoporous structure for removing the NO gas, *J. Catal.* 357 (2018) 100–107.
- [7] P. Chen, F. Wang, Z.-F. Chen, Q. Zhang, Y. Su, L. Shen, K. Yao, Y. Liu, Z. Cai, W. Lv, G. Liu, Study on the photocatalytic mechanism and detoxicity of gemfibrozil by a sunlight-driven TiO₂/carbon dots photocatalyst: the significant roles of reactive oxygen species, *Appl. Catal. B-Environ.* 204 (2017) 250–259.
- [8] J. Fu, J. Yu, C. Jiang, B. Cheng, g-C₃N₄-based heterostructured photocatalysts, *Adv. Energy Mater.* 8 (2018).
- [9] A. Pisanu, A. Speltini, B. Vigani, F. Ferrari, M. Mannini, N. Calisi, B. Cortigiani, A. Caneschi, P. Quadrelli, A. Profumo, L. Malavasi, Enhanced hydrogen photogeneration by bulk g-C₃N₄ through a simple and efficient oxidation route, *Dalton Trans.* 47 (2018) 6772–6778.
- [10] F. Wang, Y. Wang, Y. Feng, Y. Zeng, Z. Xie, Q. Zhang, Y. Su, P. Chen, Y. Liu, K. Yao, W. Lv, G. Liu, Novel ternary photocatalyst of single atom-dispersed silver and carbon quantum dots co-loaded with ultrathin g-C₃N₄ for broad spectrum photocatalytic degradation of naproxen, *Appl. Catal. B-Environ.* 221 (2018) 510–520.
- [11] W.-J. Ong, L.-L. Tan, Y.H. Ng, S.-T. Yong, S.-P. Chai, Graphitic carbon nitride (g-C₃N₄)-based photocatalysts for artificial photosynthesis and environmental remediation: are we a step closer to achieving sustainability? *Chem. Rev.* 116 (2016) 7159–7329.
- [12] F. Dong, L. Wu, Y. Sun, M. Fu, Z. Wu, S.C. Lee, Efficient synthesis of polymeric g-C₃N₄ layered materials as novel efficient visible light driven photocatalysts, *J. Mater. Chem.* 21 (2011) 15171–15174.
- [13] Q. Zhang, P. Chen, C. Tan, T. Chen, M. Zhuo, Z. Xie, F. Wang, H. Liu, Z. Cai, G. Liu, W. Lv, A photocatalytic degradation strategy of PPCPs by a heptazine-based CN organic polymer (OCN) under visible light, *Environ. Sci. Nano* 5 (2018) 2325–2336.
- [14] Y. Wang, F. Wang, Y. Feng, Z. Xie, Q. Zhang, X. Jin, H. Liu, Y. Liu, W. Lv, G. Liu, Facile synthesis of carbon quantum dots loaded with mesoporous g-C₃N₄ for synergistic absorption and visible light photodegradation of fluoroquinolone antibiotics, *Dalton Trans.* 47 (2018) 1284–1293.
- [15] Z. Xie, Y. Feng, F. Wang, D. Chen, Q. Zhang, Y. Zeng, W. Lv, G. Liu, Construction of carbon dots modified MoO₃/g-C₃N₄ Z-scheme photocatalyst with enhanced visible-light photocatalytic activity for the degradation of tetracycline, *Appl. Catal. B-Environ.* 229 (2018) 96–104.
- [16] R. Ma, S. Zhang, T. Wen, P. Gu, L. Li, G. Zhao, F. Niu, Q. Huang, Z. Tang, X. Wang, A critical review on visible-light-response CeO₂-based photocatalysts with enhanced photooxidation of organic pollutants, *Catal. Today* (2018).
- [17] S. Zhang, P. Gu, R. Ma, C. Luo, T. Wen, G. Zhao, W. Cheng, X. Wang, Recent developments in fabrication and structure regulation of visible-light-driven g-C₃N₄-based photocatalysts towards water purification: a critical review, *Catal. Today* (2018).
- [18] J. Xue, S. Ma, Y. Zhou, Z. Zhang, M. He, Facile photochemical synthesis of Au/Pt/g-C₃N₄ with plasmon-enhanced photocatalytic activity for antibiotic degradation, *ACS Appl. Mater. Interfaces* 7 (2015) 9630–9637.
- [19] Q. Liu, Y. Guo, Z. Chen, Z. Zhang, X. Fang, Constructing a novel ternary Fe(III)/graphene/g-C₃N₄ composite photocatalyst with enhanced visible-light driven photocatalytic activity via interfacial charge transfer effect, *Appl. Catal. B-Environ.* 183 (2016) 231–241.
- [20] J. Qin, J. Huo, P. Zhang, J. Zeng, T. Wang, H. Zeng, Improving the photocatalytic hydrogen production of Ag/g-C₃N₄ nanocomposites by dye-sensitization under visible light irradiation, *Nanoscale* 8 (2016) 2249–2259.
- [21] Y. Wang, S. Zhao, Y. Zhang, J. Fang, Y. Zhou, S. Yuan, C. Zhang, W. Chen, One-pot synthesis of K-doped g-C₃N₄ nanosheets with enhanced photocatalytic hydrogen production under visible-light irradiation, *Appl. Surf. Sci.* 440 (2018) 258–265.
- [22] S.C. Yan, Z.S. Li, Z.G. Zou, Photodegradation of rhodamine B and methyl orange over boron-doped g-C₃N₄ under visible light irradiation, *Langmuir* 26 (2010) 3894–3901.
- [23] Y. Wang, Y. Di, M. Antonietti, H. Li, X. Chen, X. Wang, Excellent visible-light photocatalysis of fluorinated polymeric carbon nitride solids, *Chem. Mater.* 22 (2010) 5119–5121.
- [24] G. Dong, K. Zhao, L. Zhang, Carbon self-doping induced high electronic conductivity and photoreactivity of g-C₃N₄, *Chem. Commun.* 48 (2012) 6178–6180.
- [25] M.A. Mohamed, M.F.M. Zain, L. Jeffery Minguo, M.B. Kassim, N.A. Saidina Amin, W.N.W. Salleh, M.N.I. Salehmin, M.F. Md Nasir, Z.A. Mohd Hir, Constructing biotemplated 3D porous microtubular C-doped g-C₃N₄ with tunable band structure and enhanced charge carrier separation, *Appl. Catal. B* 236 (2018) 265–279.
- [26] M. Ballardini, E.I. Garcia-Lopez, G. Marci, I. Krivtsov, J.R. Garcia, L. Palmisano, Selective photocatalytic oxidation of aromatic alcohols in water by using P-doped g-C₃N₄, *Appl. Catal. B-Environ.* 220 (2018) 222–233.
- [27] D. Chen, J. Liu, Z. Jia, J. Fang, F. Yang, Y. Tang, K. Wu, Z. Liu, Z. Fang, Efficient visible-light-driven hydrogen evolution and Cr(VI) reduction over porous P and Mo co-doped g-C₃N₄ with feeble N vacancies photocatalyst, *J. Hazard. Mater.* 361 (2018) 294–304.
- [28] B. Zhu, P. Xia, Y. Li, W. Ho, J. Yu, Fabrication and photocatalytic activity enhanced mechanism of direct Z-scheme g-C₃N₄/Ag₂WO₄ photocatalyst, *Appl. Surf. Sci.* 391 (2017) 175–183.
- [29] M. Sereydych, T.J. Bandoz, Nitrogen enrichment of S-doped nanoporous carbon by g-C₃N₄: insight into photosensitivity enhancement, *Carbon* 107 (2016) 895–906.
- [30] Z.-F. Huang, J. Song, L. Pan, Z. Wang, X. Zhang, J.-J. Zou, W. Mi, X. Zhang, L. Wang, Carbon nitride with simultaneous porous network and O-doping for efficient solar-energy-driven hydrogen evolution, *Nano Energy* 12 (2015) 646–656.
- [31] J. Fu, B. Zhu, C. Jiang, B. Cheng, W. You, J. Yu, Hierarchical porous O-doped g-C₃N₄ with enhanced photocatalytic CO₂ reduction activity, *Small* 13 (2017).
- [32] Y. Zhou, L. Zhang, J. Liu, X. Fan, B. Wang, M. Wang, W. Ren, J. Wang, M. Li, J. Shi, Brand new P-doped g-C₃N₄: enhanced photocatalytic activity for H₂ evolution and Rhodamine B degradation under visible light, *J. Mater. Chem. A* 3 (2015) 3862–3867.
- [33] J. Li, M.S. Safarzadeh, M.S. Moats, J.D. Miller, K.M. LeVier, M. Dietrich, R.Y. Wan, Thiocyanate hydrometallurgy for the recovery of gold. Part I: chemical and thermodynamic considerations, *Hydrometallurgy* 113 (2012) 1–9.
- [34] L.J. Fang, X.L. Wang, J.J. Zhao, Y.H. Li, Y.L. Wang, X.L. Du, Z.F. He, H.D. Zeng, H.G. Yang, One-step fabrication of porous oxygen-doped g-C₃N₄ with feeble nitrogen vacancies for enhanced photocatalytic performance, *Chem. Commun.* 52 (2016) 14408–14411.
- [35] C.C. Hu, W.Z. Hung, M.S. Wang, P.J. Lu, Phosphorus and sulfur codoped g-C₃N₄ as an efficient metal-free photocatalyst, *Carbon* 127 (2018) 374–383.
- [36] G.W.T.M.J. Frisch, H.B. Schlegel, G.E. Scuseria, M.A. Robb, J.R. Cheeseman, G. Scalmani, V. Barone, B. Mennucci, G.A. Petersson, H. Nakatsuji, M. Caricato, X. Li, H.P. Hrathian, A.F. Izmaylov, J. Bloino, G. Zheng, J.L. Sonnenberg, M. Hada, M. Ehara, K. Toyota, R. Fukuda, J. Hasegawa, M. Ishida, T. Nakajima, Y. Honda, O. Kitao, H. Nakai, T. Vreven, J.A. Montgomery Jr., J.E. Peralta, F. Ogliaro, M. Bearpark, J.J. Heyd, E. Brothers, K.N. Kudin, V.N. Staroverov, R. Kobayashi, J. Normand, K. Raghavachari, A. Rendell, J.C. Burant, S.S. Iyengar, J. Tomasi, M. Cossi, N. Rega, J.M. Millam, M. Klene, J.E. Knox, J.B. Cross, V. Bakken, C. Adamo, J. Jaramillo, R. Gomperts, R.E. Stratmann, O. Yazyev, A.J. Austin, R. Cammi, C. Pomelli, J.W. Ochterski, R.L. Martin, K. Morokuma, V.G. Zakrzewski, G.A. Voth, P. Salvador, J.J. Dannenberg, S. Dapprich, A.D. Daniels, Ö. Farkas, J.B. Foresman, J.V. Ortiz, J. Cioslowski, D.J. Fox, Gaussian 09, Gaussian Inc, Wallingford CT, 2009.
- [37] W. Yang, W.J. Mortier, The use of global and local molecular parameters for the analysis of the gas-phase basicity of amines, *J. Am. Chem. Soc.* 108 (1986) 5708–5711.
- [38] L. Jiang, X. Yuan, G. Zeng, X. Chen, Z. Wu, J. Liang, J. Zhang, H. Wang, H. Wang, Phosphorus- and sulfur-codoped g-C₃N₄: facile preparation, mechanism insight, and application as efficient photocatalyst for tetracycline and methyl orange degradation under visible light irradiation, *ACS Sustain. Chem. Eng.* 5 (2017) 5831–5841.
- [39] J. Gao, Y. Zhou, Z. Li, S. Yan, N. Wang, Z. Zou, High-yield synthesis of millimetre-long, semiconducting carbon nitride nanotubes with intense photoluminescence emission and reproducible photoconductivity, *Nanoscale* 4 (2012) 3687–3692.
- [40] M.A. Mohamed, J. Jaafar, A.F. Ismail, M.H.D. Othman, M.A. Rahman, Chapter 1 – Fourier transform infrared (FTIR) spectroscopy, in: N. Hilal, A.F. Ismail, T. Matsuura, D. Oatley-Radcliffe (Eds.), *Membrane Characterization*, Elsevier, 2017, pp. 3–29.
- [41] C. Liu, H. Huang, W. Cui, F. Dong, Y. Zhang, Band structure engineering and efficient charge transport in oxygen substituted g-C₃N₄ for superior photocatalytic hydrogen evolution, *Appl. Catal. B-Environ.* 230 (2018) 115–124.
- [42] B. Zhu, P. Xia, W. Ho, J. Yu, Isoelectric point and adsorption activity of porous g-C₃N₄, *Appl. Surf. Sci.* 344 (2015) 188–195.
- [43] Y. Zhou, L. Zhang, J. Liu, X. Fan, B. Wang, M. Wang, W. Ren, J. Wang, M. Li, J. Shi, Brand new P-doped g-C₃N₄: enhanced photocatalytic activity for H₂ evolution and Rhodamine B degradation under visible light, *J. Mater. Chem. A* 3 (2015) 3862–3867.
- [44] S. Guo, Z. Deng, M. Li, B. Jiang, C. Tian, Q. Pan, H. Fu, Phosphorus-doped carbon nitride tubes with a layered micro-nanostructure for enhanced visible-light photocatalytic hydrogen evolution, *Angew. Chem.-Int. Ed.* 55 (2016) 1830–1834.
- [45] Y. Cui, H. Wang, C. Yang, M. Li, Y. Zhao, F. Chen, Post-activation of in situ B-F codoped g-C₃N₄ for enhanced photocatalytic H₂ evolution, *Appl. Surf. Sci.* 441 (2018) 621–630.
- [46] Q. Tay, P. Kanhere, C.F. Ng, S. Chen, S. Chakraborty, A.C.H. Huan, T.C. Sum, R. Ahuja, Z. Chen, Defect engineered g-C₃N₄ for efficient visible light photocatalytic hydrogen production, *Chem. Mater.* 27 (2015) 4930–4933.
- [47] B. Chai, J. Yan, C. Wang, Z. Ren, Y. Zhu, Enhanced visible light photocatalytic degradation of Rhodamine B over phosphorus doped graphitic carbon nitride, *Appl. Surf. Sci.* 391 (2017) 376–383.
- [48] J. Luo, X. Zhou, L. Ma, X. Xu, Enhancing visible-light photocatalytic activity of g-C₃N₄ by doping phosphorus and coupling with CeO₂ for the degradation of methyl orange under visible light irradiation, *RSC Adv.* 5 (2015) 68728–68735.
- [49] L. Ming, H. Yue, L. Xu, F. Chen, Hydrothermal synthesis of oxidized g-C₃N₄ and its regulation of photocatalytic activity, *J. Mater. Chem. A* 2 (2014) 19145–19149.
- [50] J. Li, B. Shen, Z. Hong, B. Lin, B. Gao, Y. Chen, A facile approach to synthesize novel oxygen-doped g-C₃N₄ with superior visible-light photoreactivity, *Chem. Commun.* 48 (2012) 12017–12019.
- [51] Y. Zeng, X. Liu, C. Liu, L. Wang, Y. Xia, S. Zhang, S. Luo, Y. Pei, Scalable one-step production of porous oxygen-doped g-C₃N₄ nanorods with effective electron

- separation for excellent visible-light photocatalytic activity, *Appl. Catal. B-Environ.* 224 (2018) 1–9.
- [52] Y. Wang, M.K. Bayazit, S.J.A. Moniz, Q. Ruan, C.C. Lau, N. Martsinovich, J. Tang, Linker-controlled polymeric photocatalyst for highly efficient hydrogen evolution from water, *Energy Environ. Sci.* 10 (2017) 1643–1651.
- [53] B. Jurgens, E. Irran, J. Senker, P. Kroll, H. Muller, W. Schnick, Melem (2,5,8-triamino-tri-s-triazine), an important intermediate during condensation of melamine rings to graphitic carbon nitride: Synthesis, structure determination by X-ray powder diffractometry, solid-state NMR, and theoretical studies, *J. Am. Chem. Soc.* 125 (2003) 10288–10300.
- [54] X.L. Wang, W.Q. Fang, H.F. Wang, H. Zhang, H. Zhao, Y. Yao, H.G. Yang, Surface hydrogen bonding can enhance photocatalytic H₂ evolution efficiency, *J. Mater. Chem. A* 1 (2013) 14089–14096.
- [55] J. Zhang, G. Zhang, X. Chen, S. Lin, L. Moehlmann, G. Dolega, G. Lipner, M. Antonietti, S. Blechert, X. Wang, Co-monomer control of carbon nitride semiconductors to optimize hydrogen evolution with visible light, *Angew. Chem.-Int. Ed.* 51 (2012) 3183–3187.
- [56] W.S. Zhu, X. Gao, Q. Li, H.P. Li, Y.H. Chao, M.J. Li, S.M. Mahurin, H.M. Li, H.Y. Zhu, S. Dai, Controlled gas exfoliation of boron nitride into few-layered nanosheets, *Angew. Chem. Int. Ed.* 55 (2016) 10766–10770.
- [57] S.C. Yan, Z.S. Li, Z.G. Zou, Photodegradation performance of g-C₃N₄ fabricated by directly heating melamine, *Langmuir* 25 (2009) 10397–10401.
- [58] X. Shi, M. Fujitsuka, Z. Lou, P. Zhang, T. Majima, In situ nitrogen-doped hollow-TiO₂/g-C₃N₄ composite photocatalysts with efficient charge separation boosting water reduction under visible light, *J. Mater. Chem. A* 5 (2017) 9671–9681.
- [59] Y. He, L. Zhang, X. Wang, Y. Wu, H. Lin, L. Zhao, W. Weng, H. Wan, M. Fan, Enhanced photodegradation activity of methyl orange over Z-scheme type MoO₃-g-C₃N₄ composite under visible light irradiation, *RSC Adv.* 4 (2014) 13610–13619.
- [60] L. Huang, H. Xu, R. Zhang, X. Cheng, J. Xia, Y. Xu, H. Li, Synthesis and characterization of g-C₃N₄/MoO₃ photocatalyst with improved visible-light photoactivity, *Appl. Surf. Sci.* 283 (2013) 25–32.
- [61] J. Zhang, M. Zhang, R.-Q. Sun, X. Wang, A facile band alignment of polymeric carbon nitride semiconductors to construct isotype heterojunctions, *Angew. Chem.-Int. Ed.* 51 (2012) 10145–10149.
- [62] J. Ran, T.Y. Ma, G. Gao, X.-W. Du, S.Z. Qiao, Porous P-doped graphitic carbon nitride nanosheets for synergistically enhanced visible-light photocatalytic H₂ production, *Energy Environ. Sci.* 8 (2015) 3708–3717.
- [63] P. Qiu, C. Xu, H. Chen, F. Jiang, X. Wang, R. Lu, X. Zhang, One step synthesis of oxygen doped porous graphitic carbon nitride with remarkable improvement of photo-oxidation activity: role of oxygen on visible light photocatalytic activity, *Appl. Catal. B* 206 (2017) 319–327.
- [64] G. Zhang, M. Zhang, X. Ye, X. Qiu, S. Lin, X. Wang, Iodine modified carbon nitride semiconductors as visible light photocatalysts for hydrogen evolution, *Adv. Mater.* 26 (2014) 805–809.
- [65] S. Zhang, Y. Liu, P. Gu, R. Ma, T. Wen, G. Zhao, L. Li, Y. Ai, C. Hu, X. Wang, Enhanced photodegradation of toxic organic pollutants using dual-oxygen-doped porous g-C₃N₄: mechanism exploration from both experimental and DFT studies, *Appl. Catal. B* 248 (2019) 1–10.
- [66] S.Y. Chen, R. Yan, X.L. Zhang, K. Hu, Z.J. Li, M. Humayun, Y. Qu, L.Q. Jing, Photogenerated electron modulation to dominantly induce efficient 2,4-dichlorophenol degradation on BiOBr nanoplates with different phosphate modification, *Appl. Catal. B* 209 (2017) 320–328.
- [67] H. Huang, Y. He, X. Li, M. Li, C. Zeng, F. Dong, X. Du, T. Zhang, Y. Zhang, Bi₂O₂(OH)(NO₃) as a desirable Bi₂O₂ (2+) layered photocatalyst: strong intrinsic polarity, rational band structure and 001 active facets co-beneficial for robust photooxidation capability, *J. Mater. Chem. A* 3 (2015) 24547–24556.
- [68] S. Zhang, S. Song, P. Gu, R. Ma, D. Wei, G. Zhao, T. Wen, R. Jehan, B. Hu, X. Wang, Visible-light-driven activation of persulfate over cyano and hydroxyl group co-modified mesoporous g-C₃N₄ for boosting bisphenol A degradation, *J. Mater. Chem. A* 7 (2019) 5552–5560.
- [69] B. De Witte, H. Van Langenhove, K. Hemelsoet, K. Demeestere, P. De Wispelaere, V. Van Speybroeck, J. Dewulf, Levofloxacin ozonation in water: rate determining process parameters and reaction pathway elucidation, *Chemosphere* 76 (2009) 683–689.
- [70] B. Yang, Z. Cheng, Q. Tang, Z. Shen, Nitrogen transformation of 41 organic compounds during SCWO: A study on TN degradation rate, N-containing species distribution and molecular characteristics, *Water Res.* 140 (2018) 167–180.
- [71] J. Olah, C. Van Alsenoy, A.B. Sannigrahi, Condensed Fukui functions derived from stockholder charges: assessment of their performance as local reactivity descriptors, *J. Phys. Chem. A* 106 (2002) 3885–3890.
- [72] C. Wang, P. Shi, X. Cai, Q. Xu, X. Zhou, X. Zhou, D. Yang, J. Fan, Y. Min, H. Ge, W. Yao, Synergistic effect of Co₃O₄ nanoparticles and graphene as catalysts for peroxymonosulfate-based orange II degradation with high oxidant utilization efficiency, *J. Phys. Chem. C* 120 (2016) 336–344.
- [73] X.-J. Wen, C.-G. Niu, L. Zhang, C. Liang, G.-M. Zeng, A novel Ag₂O/CeO₂ heterojunction photocatalysts for photocatalytic degradation of enrofloxacin: possible degradation pathways, mineralization activity and an in depth mechanism insight, *Appl. Catal. B-Environ.* 221 (2018) 701–714.
- [74] T. Chen, Q. Zhang, Z. Xie, C. Tan, P. Chen, Y. Zeng, F. Wang, H. Liu, Y. Liu, G. Liu, W. Lv, Carbon nitride modified hexagonal boron nitride interface as highly efficient blue LED light-driven photocatalyst, *Appl. Catal. B-Environ.* 238 (2018) 410–421.
- [75] C. Jiang, Y. Ji, Y. Shi, J. Chen, T. Cai, Sulfate radical-based oxidation of fluoroquinolone antibiotics: kinetics, mechanisms and effects of natural water matrices, *Water Res.* 106 (2016) 507–517.